Effect of Si Level on the Evolution of Zr-bearing Dispersoids and the Related Hot Deformation and Recrystallization Behaviors in Al-Si-Mg 6xxx Alloys

A. Elasheri [a], E. M. Elgallad [a,], N. Parson [b], and X.-G. Chen [a,]**

[a] Department of Applied Science, University of Quebec at Chicoutimi, Saguenay (QC), Canada G7H 2B1

*(*Corresponding authors: Emad_Elgallad@uqac.ca and XGrant_Chen@uqac.ca)*

[b] Arvida Research and Development Centre, Rio Tinto Aluminium, Saguenay (QC), Canada G7S 4K8

Abstract

The precipitation behavior of Zr-bearing dispersoids is investigated in Al-Si-Mg 6xxx alloys with different Si levels (0.4, 0.7, and 1.0 wt%) at three homogenization temperatures (450, 500, and 550 °C). The hot deformation behavior is studied using uniaxial compression tests at different Zener-Hollomon parameters. The microstructure evolution during hot deformation and post-deformation annealing is evaluated using the electron backscatter diffraction technique. The results show a significant influence of the Si level and homogenization temperature on the precipitation of two types of Zr-bearing dispersoids. Si promotes the precipitation of both spherical $L1_2$-Al_3Zr and elongated DO_{22}-$(Al,Si)_3(Zr,Ti)$ dispersoids during low-temperature homogenization. However, it accelerates the transformation of Zr dispersoids from $L1_2$ to DO_{22} at high homogenization temperature. The flow stress is more influenced by the solid solution level and hot deformation parameters rather than by the dispersoid distribution. The fine dense $L1_2$-Al_3Zr dispersoids provide higher recrystallization resistance during post-deformation annealing compared to the large elongated DO_{22}-$(Al,Si)_3(Zr,Ti)$ dispersoids. Owing to the uniform distribution of dispersoids and limited dispersoid free zones, the high Si alloy (1.0%) exhibits the best recrystallization resistance among the three alloys studied.

Keywords: Al-Mg-Si 6xxx alloys, Zr-bearing dispersoids, Hot Deformation, Recrystallization Resistance

1. Introduction

Owing to the variety of mechanical properties offered by Al-Mg-Si 6xxx alloys, they are used in a wide range of applications, from light architectural uses to high-stress structural components in the automobile, construction, and marine industries.[1, 2] These alloys are commonly used in the form of extruded profiles acquiring nearly 90% of all aluminum extrusion products since they can be extruded at higher speeds than other alloy series with less surface quality problems.[3] Hence, hot extrusion is one of the main plastic deformation processes for 6xxx alloys to achieve the desirable and complex geometric profiles. However, maintaining a fibrous grain structure is essential to improve strength, fatigue, and toughness properties.[4] Also, controlling the grain structure is of great importance for adequate performance during post-deformation heat treatment such as annealing or solution treatment.[5] In this regard, adjusting the alloy chemistry, homogenization treatment, and hot deformation parameters are the main approaches.

The addition of transition elements that have limited solubility and diffusivity in the aluminum matrix is one of the effective methods to control the grain structure during and after hot deformation in 6xxx alloys.[6, 7] Among those elements, Zr has received much attention in recent years as an addition to aluminum alloys,[4, 8, 9] due to its very low diffusivity and excellent lattice mismatch with the aluminum matrix. [10] It has been proven to positively affect the flow stress and recrystallization resistance for several aluminum alloys.[8, 11, 12] This can be achieved by introducing a high density of coherent $L1_2$-Al_3Zr dispersoids that precipitated during homogenization at relatively low-temperature.[8] However, Zr alone has not been widely used in 6xxx alloys to inhibit the recrystallization, and it is often combined with other elements such as Cr or Sc. For instance, Meng et al.[13] observed a strong inhibition effect on dynamic recrystallization after adding 0.15wt% Zr into Al-Mg-Si-Cu-Cr alloy. Also, Birol reported that the combined

addition of Zr and Cr had a positive impact on the recrystallization resistance of 6082 alloys.[4] Moreover, better recrystallization resistance was reported in Al-Mg–Si-Sc-Zr alloy compared to Al-Mg-Si–Mn–Cr.[14]

The presence of a considerable amount of silicon could influence the nucleation rate and structure of Al_3Zr at high temperatures. The nucleation of $L1_2$-Al_3Zr was reported to be enhanced by Si, and the silicon-vacancy clusters that form by attractive binding energy may act as heterogeneous sites for Zr dispersoids.[15] Si was also reported to reduce the peak-aging time of Al_3Zr dispersoids by improving the Zr diffusion kinetics in the Al matrix in the temperature range of 300 to 400 °C.[16, 17] In addition, Si was reported to stabilize DO_{22}-$(Al,Si)_3Zr$ at the expense of the metastable $L1_2$-Al_3Zr via phase transformation during high-temperature homogenization.[13, 17, 18] This transformation occurs by substituting Al by a small amount of Si and changing the crystal structure of $L1_2$ to DO_{22} instead of the stable DO_{23} that forms in the absence of Si.[18] $L1_2$-Al_3Zr has spherical morphology with a small diameter ranging from 8 to 60 nm. On the other side, the tetragonal DO_{22} has a rod-like morphology with a much larger size, around 1.5 um long and 0.5 um wide.[13, 17]

Dynamic recovery (DRV) and dynamic recrystallization (DRX) are the common softening mechanisms in aluminum alloys during thermomechanical processing. DRV is the most frequently encountered due to aluminum's high stacking fault energy, high dislocation mobility, and low grain boundary mobility.[19] While DRX can occur by the formation of new grains at particular deformation conditions (i.e., deformation temperature and strain rate). The Zener-Hollomon parameter (Z) describes the combined effect of the temperature and strain rate on the flow stress and the microstructure evolution during hot deformation.[20] On the other hand, 6xxx alloys are usually subjected to a post-deformation heat treatment (annealing or solutionizing and ageing) to

achieve the appropriate mechanical properties. Static recrystallization can occur during post-deformation heat treatment by migration of grain boundaries and the formation of new grains.[21] However, recrystallization can be significantly inhibited by the interaction between the thermally stable dispersoids and grain boundaries, which is commonly described by the Zener drag force (P_z).[22]

As mentioned above, Si plays a substantial role in the precipitation of Zr-bearing dispersoids in 6xxx alloys, which, in turn, can significantly influence the hot deformation and recrystallization resistance. However, there is a lack of literature on how and at which level Si affects the precipitation of Zr-bearing dispersoids in 6xxx alloys. The present work was undertaken to study the evolution of Zr-bearing dispersoids in 6xxx alloys at different levels of Si (0.4 -1.0 wt%) during homogenization. In addition, the effects of this evolution on the hot deformation behavior and recrystallization resistance during post-deformation heat treatment were investigated.

2. Experimental procedures

Three 6xxx alloys with different Si levels (0.4, 0.7 and 1.0 wt%) were prepared. The chemical compositions of the experimental alloys analyzed by optical emission spectroscopy are listed in **Table 1**. Because the major hardening precipitates in the 6xxx alloys are β″-Mg_5Si_6 precipitates with a Mg:Si atomic ratio of around 1:1,[23, 24] the Mg level was adjusted to maintain the atomic ratio between Mg and Si at 1:1 for the three alloys. The alloys were prepared using pure Al (99.7 wt%) and pure Mg (99.8 wt%) as well as Al-50 wt% Si, Al-25 wt% Fe, and Al-15 wt% Zr master alloys. The materials were melted using an electrical resistance furnace and cast into a permanent steel mold preheated to 250 °C to obtain rectangular ingots with a dimension of 30 mm × 40 mm × 80 mm. The cast ingots were homogenized at three temperatures (450, 500, and 550 °C) with a

heating ramp rate of 100 °C/h and soaked for 5 h followed by water quenching to room temperature.

For microstructural investigation, samples were cut from the homogenized ingots and prepared using standard metallographic procedures. The dispersoids were observed using optical microscopy (Nikon, Eclipse ME600) and scanning electron microscopy (SEM, JEOL-6480LV) after etching with 0.5% HF for 60 s. A transmission electron microscope (TEM, JEM−2100) operated at 200 kV was used to examine the Zr-bearing dispersoids in detail. The TEM samples were electropolished using a twin-jet electropolisher operated at 20V and -20 ^{o}C with 30 vol.% nitric acid and 70 vol.% methanol. The samples were observed in the bright field mode near <001> zone axis of α-Al matrix, while the dark field mode was used for the observation of $L1_2$ structured dispersoids using their superlattice reflection. The TEM foil thickness was measured by the Kossel-Kossel-Möllenstedt (K-M) fringes with the convergent electron beam diffraction method. [25] By Using an Image analyzer, the average size and number density of tiny Al_3Zr dispersoids were measured based on TEM images, whereas SEM images were used in the case of large elongated dispersoids (>100 nm). The number density of dispersoids represents the number of dispersoids per unit area in the case of the SEM-image-based analysis or per unit volume for the TEM-image-based analysis taking into consideration the TEM foil thickness. In order to estimate the solid solution level in the aluminum matrix after homogenization, electrical conductivity measurements were performed using a Simgascope SMP 10 device at room temperature. Six measurements were recorded on each sample, and the mean value was reported.

Table 1. Chemical composition (wt.%) of the experimental alloys.

Alloy ID	Si	Mg	Fe	Zr	Ti	Al
0.4Si	**0.39**	0.35	0.16	0.15	0.13	Bal.
0.7Si	**0.71**	0.64	0.15	0.14	0.12	Bal.
1.0Si	**0.99**	0.89	0.18	0.15	0.14	Bal.

Uniaxial hot compression tests were performed on a Gleeble 3800 thermomechanical simulator using cylindrical samples with a diameter of 10 mm and length of 15 mm. The compression tests involved heating the samples up to the deformation temperature with a heating rate of 2 ^{o}C/s and then holding for 3 minutes to ensure a uniform temperature. Three deformation conditions (350°C, 1.0 s^{-1}, 400°C, 0.1 s^{-1} and 450°C, 0.001 s^{-1}) were selected representing high-, medium- and low-Z conditions, respectively. The samples were deformed to a true strain of 0.7, followed by water quenching to retain the deformed microstructure. Post-deformation annealing was performed at 500 ^{o}C and 540 ^{o}C for 1 h for selected homogenization conditions to study the static recrystallization resistance.

The microstructures after deformation and after annealing were characterized using the electron backscatter diffraction (EBSD) technique. The EBSD samples were sectioned parallel to the deformation axis along the centerline direction and then carefully polished to obtain high indexing quality. For an accurate comparison, the central region of the samples was examined for all conditions. All-Euler orientation maps were used with a step size of 1 μm for grain structure. For the subgrain size measurements, a line scan was performed using a step size of 0.1 μm. The low angle boundaries (2-5°), medium angle boundaries (5-15°), high angle boundaries (>15°), and the original grain boundaries (>30°) were presented by white, green, thin black, and solid black lines respectively. Sub-grain boundaries are characterized with misorientations of 2–15°, while the grain boundaries are those with misorientation angles above 15°. All misorientation angles below 2° were not considered to avoid the noise caused by the sample surface condition**.** The recrystallized grains were defined as the grains surrounded by high angle grain boundaries (> 15°) and free from internal substructures, whereas the deformed grains were those possessing a large amount of low and medium angle boundaries (2-15°) with substructures.

3. Results and discussion

3.1. As-cast microstructure

Figure 1 shows the as-cast microstructures of the studied alloys. In general, the microstructures of the three alloys consisted of the α-Al matrix, Fe-rich intermetallic phases (gray particles) and primary Mg_2Si phase (dark particles). Increasing the contents of Si and Mg (0.7Si and 1.0Si alloys) resulted in an increase in the amount and size of the primary Mg_2Si phase due to the segregation tendencies of these elements towards the interdendritic regions. [26] In addition, some equilibrium β-Mg_2Si particles were found to be precipitated close to the interdendritic regions. The high level of supersaturation of Mg and Si can promote the precipitation of these particles during cooling after solidification. Therefore, the highest amount of β-Mg_2Si particles was observed in the 1.0Si alloy (Figure 1c).

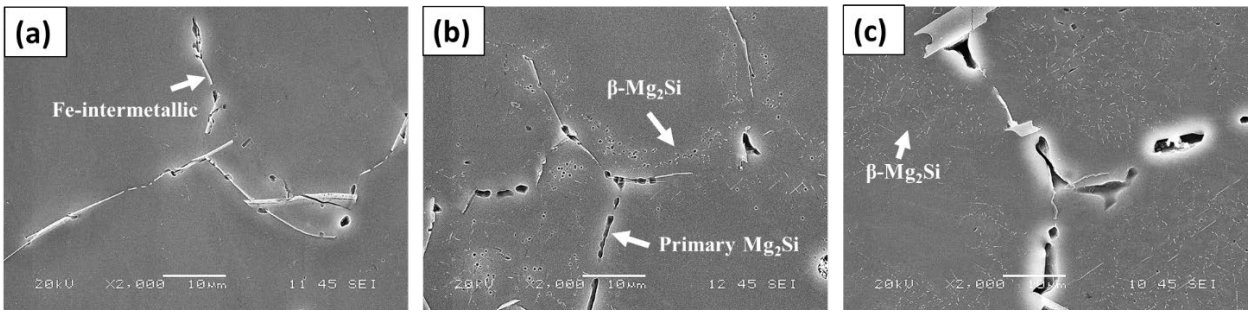

Figure 1. SEM images showing the as-cast microstructure of (a) 0.4Si, (b) 0.7Si and (c) 1.0Si alloys.

3.2. Evolution of Zr-bearing dispersoids during homogenization

Figure 2 shows the evolution of Zr-bearing dispersoids after different homogenization conditions for the 0.4Si, 0.7Si and 1.0Si alloys, which were significantly affected by the homogenization temperature and alloy composition. With increasing homogenization temperature, the size and number density of dispersoids increased for all three alloys. However, at a given homogenization temperature, the number density of dispersoids varied with the Si content. For the

0.4Si alloy (Figure 2a-c), the precipitation of dispersoids was relatively weak, resulting in a low number density. In the case of 0.7Si alloy (Figure 2d-f), a higher number density of dispersoids was generally observed compared to the 0.4Si alloy. With increasing Si to 1.0% (Figure 2g-i), a further significant increase in the number density of dispersoids was observed at all homogenization temperatures. At low homogenization temperature (450 °C), the equilibrium β-Mg_2Si particles were also precipitated and co-existed with dispersoids, as shown in the SEM images (white arrows) in **Figure 3**. In general, the β-Mg_2Si particles were larger and less dense than Zr-bearing dispersoids. However, the amount of β-Mg_2Si particles was significantly reduced with increasing the homogenization temperature and they were almost completely dissolved at 550 °C (Figure. 3d-f).

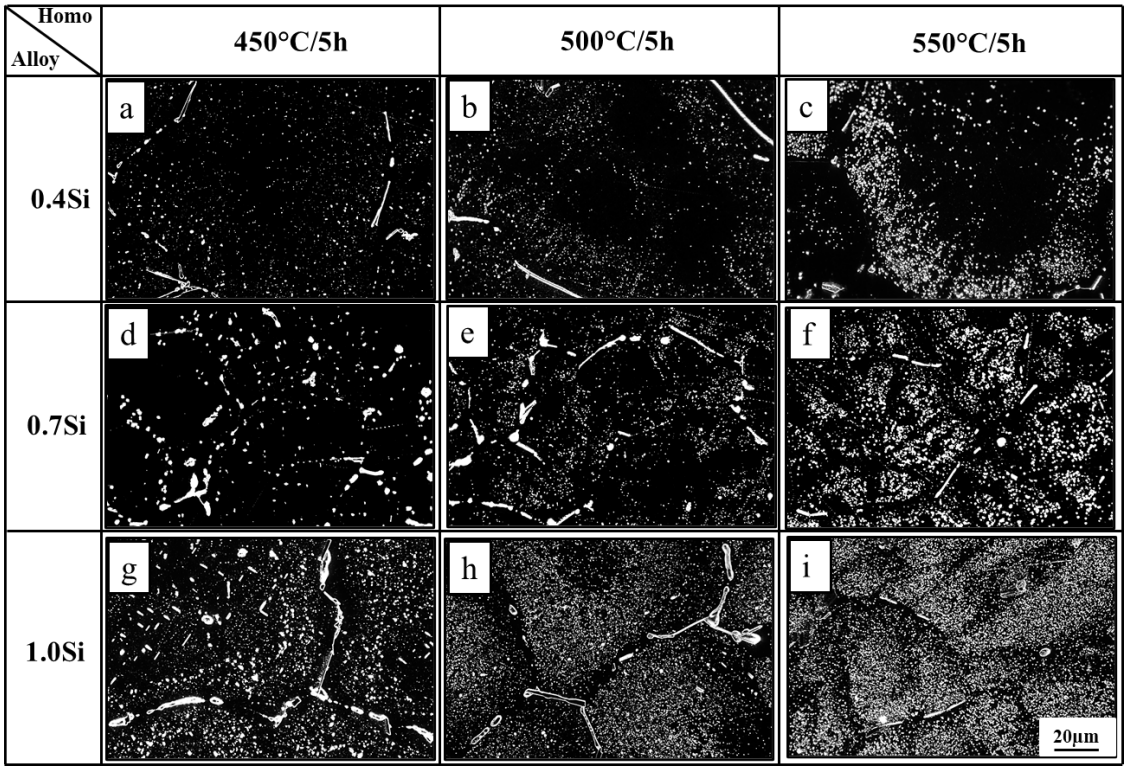

Figure 2. Dark-field optical micrographs showing the distribution of Zr-bearing dispersoids for different Si levels and homogenization temperatures.

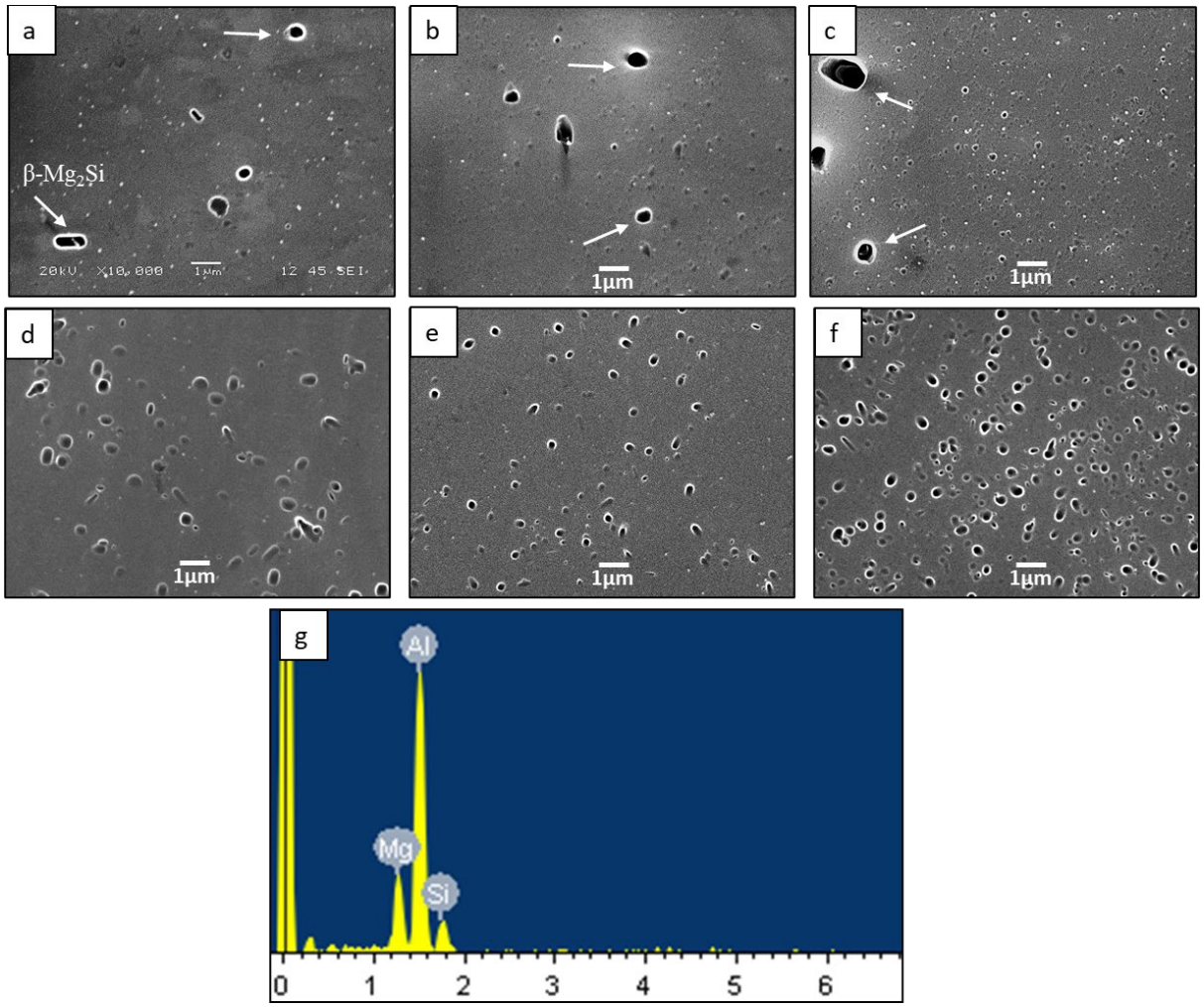

Figure 3. SEM micrographs showing Zr-dispersoids and β-Mg_2Si (large particles indicated by white arrows) after homogenization at 450°C/5h (a-c) and 550°C/5h (d-f) for 0.4Si, 0.7Si and 1.0Si alloys, and (g) SEM-EDS analysis of β-Mg_2Si particle.

TEM was used to characterize the morphology and the type of Zr-bearing dispersoids. **Figure 4** shows typical bright-field TEM images obtained after 550 °C homogenization. Two types of dispersoids were observed in the case of 0.4Si alloy (Figure 4a): large elongated dispersoids indicated by black arrows and spherical dispersoids with a much smaller size shown in the inset of Figure 4a. The same two types of dispersoids were also observed in 0.7Si alloy but with a higher density (Figure 4b). The elongated dispersoids were mainly located near grain boundaries, as shown in Figure 2c and f, while the spherical ones were located at the grain centers. Only elongated

dispersoids were observed in the 1.0Si alloy (Figure 4c), with a uniform distribution (Figure 2i). Furthermore, The corresponding selected area diffraction pattern (SADP) taken along $<001>_{Al}$ zone axis (the inset of Figure 4c) indicates that the crystal structure of the elongated dispersoids is DO_{22}, which was also reported by Litynska et al. [18]

The TEM-EDS analysis of spherical dispersoids (Figure 4d) showed that they contain only Zr, and they could therefore be identified as Al_3Zr dispersoids. However, considerable amounts of Si and Ti were detected beside Zr in the case of elongated dispersoids (Figure 4e). It has been reported that Si and Al can replace each other in Al_3Zr, resulting in a transformation from cubic $L1_2$-Al_3Zr to tetragonal DO_{22}-$(Al,Si)_3Zr$ dispersoids.[18] In addition, Ti has been proven to have a certain degree of solubility in $(Al,Si)_3Zr$.[27, 28] Therefore, it is reasonable to define the elongated dispersoids observed in this study as DO_{22}-$(Al,Si)_3(Zr,Ti)$ dispersoids.[29] It is worth noting that only DO_{22}-$(Al,Si)_3(Zr,Ti)$ dispersoids and β-Mg_2Si particles were revealed by OM and SEM (Figure 2 and 3), while the spherical dispersoids were too small to be detected, and they could only be observed with TEM (Figure 4 and 5).

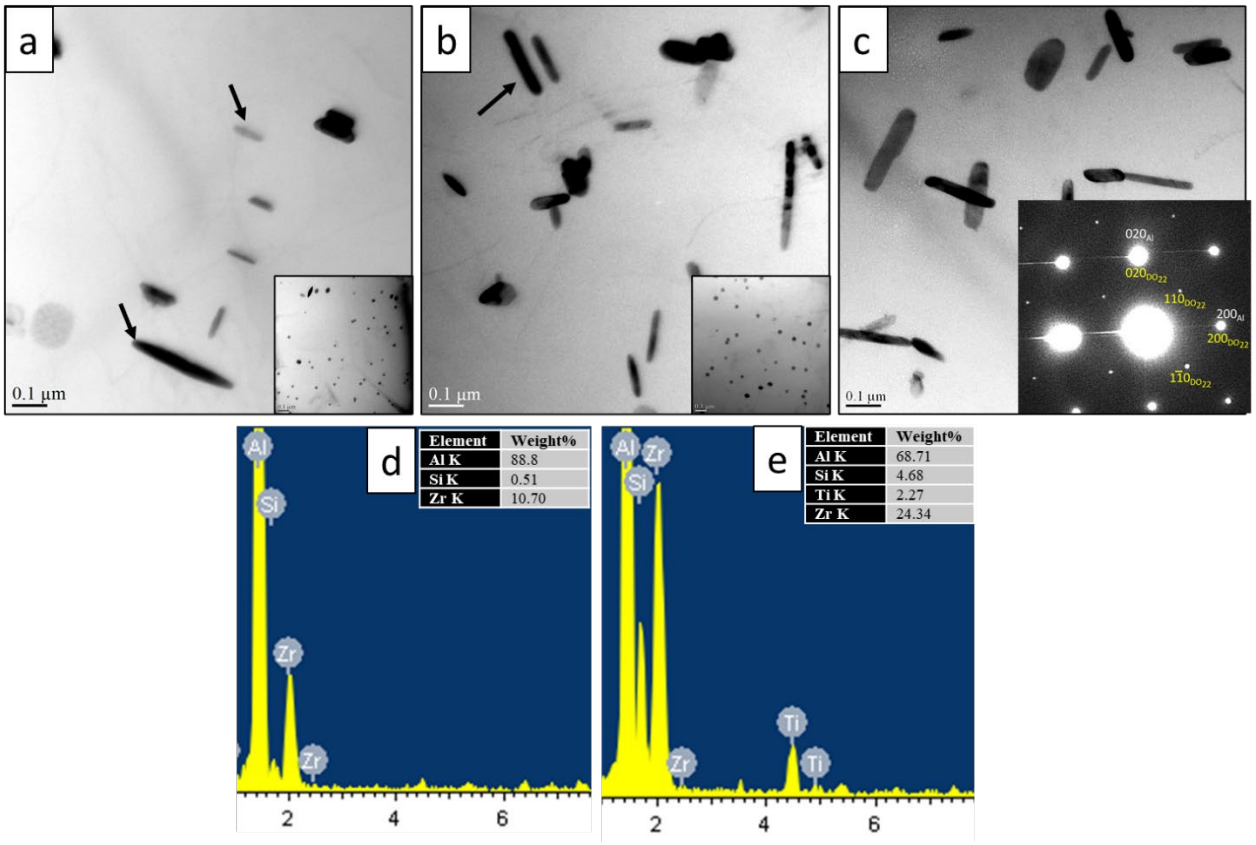

Figure 4. Bright-Field TEM images of (a) 0.4Si, (b) 0.7Si, and (c) 1.0Si alloys after homogenization at 550°C/5h and TEM-EDS analysis of (d) spherical and (e) elongated dispersoids.

TEM dark-field images were used to observe the evolution of spherical Al_3Zr dispersoids (**Figure 5**). This type of dispersoid was reported to precipitate with a large number density during low-temperature homogenization due to the high level of supersaturation of Zr in the matrix after solidification.[30] The SADP given in the inset of Figure 5c shows that this type of dispersoid has $L1_2$ cubic structure. It commonly exhibits a cube-to-cube orientation relationship with the aluminum matrix,[31] and is coherent with the matrix.[32] while the elongated DO_{22} dispersoids are typically semi-coherent or incoherent with the matrix. [33] The precipitation behavior of the $L1_2$ dispersoids was obviously different from that of the DO_{22} dispersoids. While the smallest number density of DO_{22} was observed after homogenization at 450 °C (Figure 2), the largest number

density of $L1_2$-Al_3Zr was observed at the same temperature. With increasing the homogenization temperature, the number density of $L1_2$ dispersoids significantly decreased, reaching a minimum value at 550 °C, while the dispersoid size increased. However, the change in the number density with the temperature was dependent on the alloy composition. For instance, the 0.4Si alloy (Figure 5a) exhibited a lower number density after low-temperature homogenization (450 °C) as compared to the other two alloys (0.7Si (Figure 5d) and 1.0Si (Figure 5g)), indicating the positive effect of Si on promoting the precipitation of Al_3Zr. However, increasing the Si level resulted in reduced dispersoid stability at high-temperature homogenization. After homogenization at 550 °C, the 1.0Si alloy contained almost no spherical Al_3Zr dispersoids (Figure 5i), while the 0.4Si alloy still exhibited a reasonable number density of Al_3Zr dispersoids (Figure 5c).

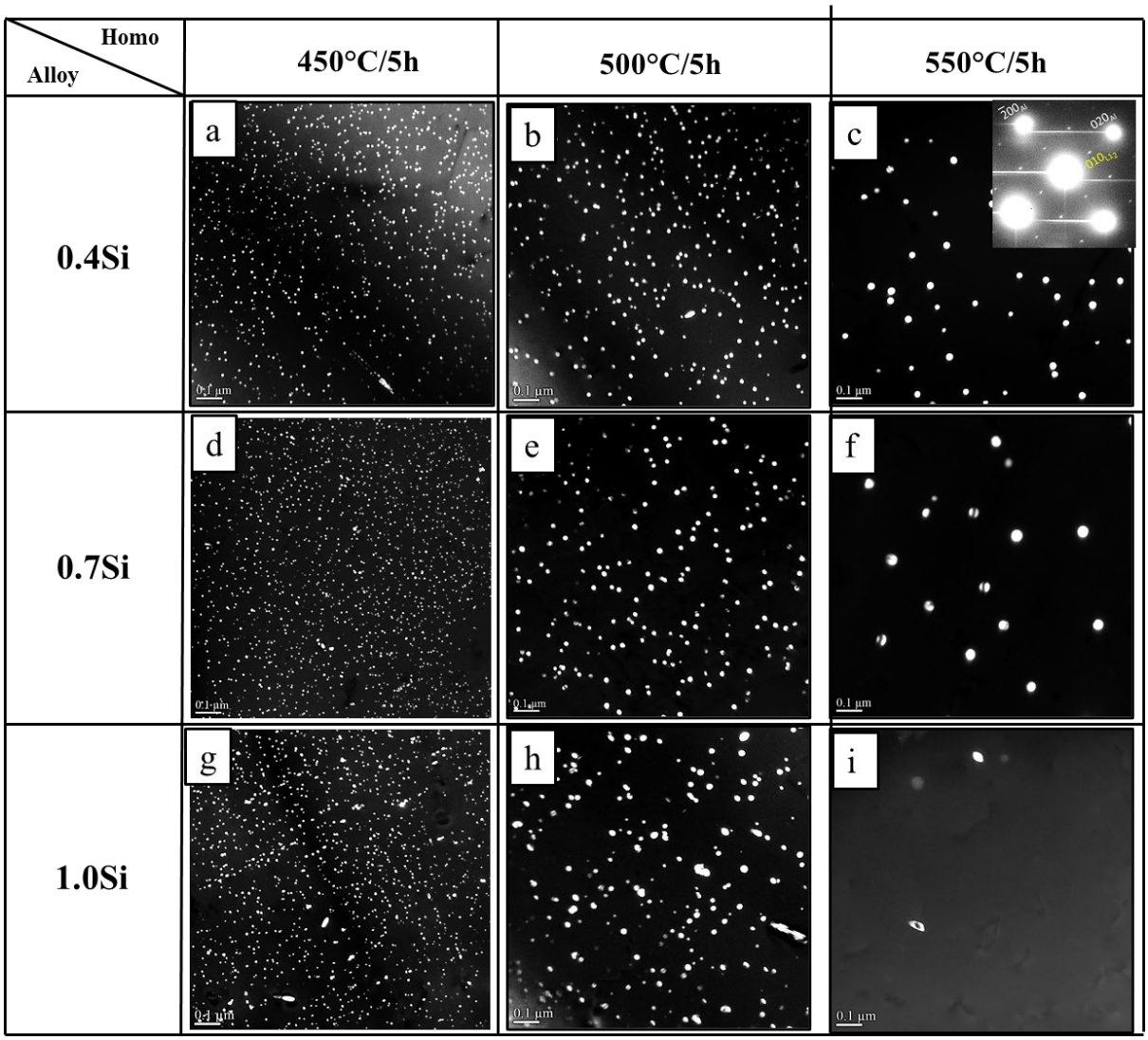

Figure 5. Dark-field TEM images for the spherical Al_3Zr dispersoids at different Si levels and homogenization temperatures.

From TEM and SEM observations, it is clear that at a given homogenization temperature, each alloy exhibits a different combination of spherical $L1_2$ and elongated DO_{22} dispersoids. **Figure 6** shows the quantitative results in terms of the number density of both spherical and elongated dispersoids in each alloy for different homogenization conditions. Due to the spatial distribution of the dispersoids, the number densities of both spherical and elongated dispersoid were measured in the dispersoid zones where the majority of the dispersoids were present. At 450°C, the number

density of the spherical Al_3Zr increased from 3918 μm^{-3} for 0.4Si to 8880 μm^{-3} for 0.7Si but decreased to 5092 μm^{-3} for 1.0Si (Figure 6a). Increasing the homogenization temperature to 500 °C significantly decreased the number densities of the spherical Al_3Zr in all three alloys and decreased the differences between these densities. After homogenization at 550 °C, the number densities further decreased and reached their minimum values (240 μm^{-3} and 144 μm^{-3}) for 0.4Si and 0.7Si, respectively, and there were almost no spherical dispersoids for 1.0 Si. In the case of the elongated DO_{22}-$(Al,Si)_3(Zr,Ti)$ dispersoids (Figure 6b), at 450°C both 0.4Si and 0.7Si exhibited a low number density (~0.8 μm^{-2}), but 1.0Si alloy almost doubled the number density (1.5 μm^{-2}). This indicates that the transformation of spherical Al_3Zr to elongated DO_{22}-$(Al,Si)_3(Zr,Ti)$ already occurred at low temperature, especially with 1.0Si. With increasing the temperature to 550 °C, the number densities of elongated dispersoids in 0.4Si and 0.7Si alloys slightly increased, while the number density in 1.0Si alloys remarkably increased, reaching its highest value of ~2.8 μm^{-2} at the expense of Al_3Zr in both 500 °C and 550 °C, indicating that the high Si level (1.0%Si) strongly promoted the transformation from Al_3Zr to DO_{22}-$(Al,Si)_3(Zr,Ti)$. In addition, the high homogenization temperature also favors this transformation.

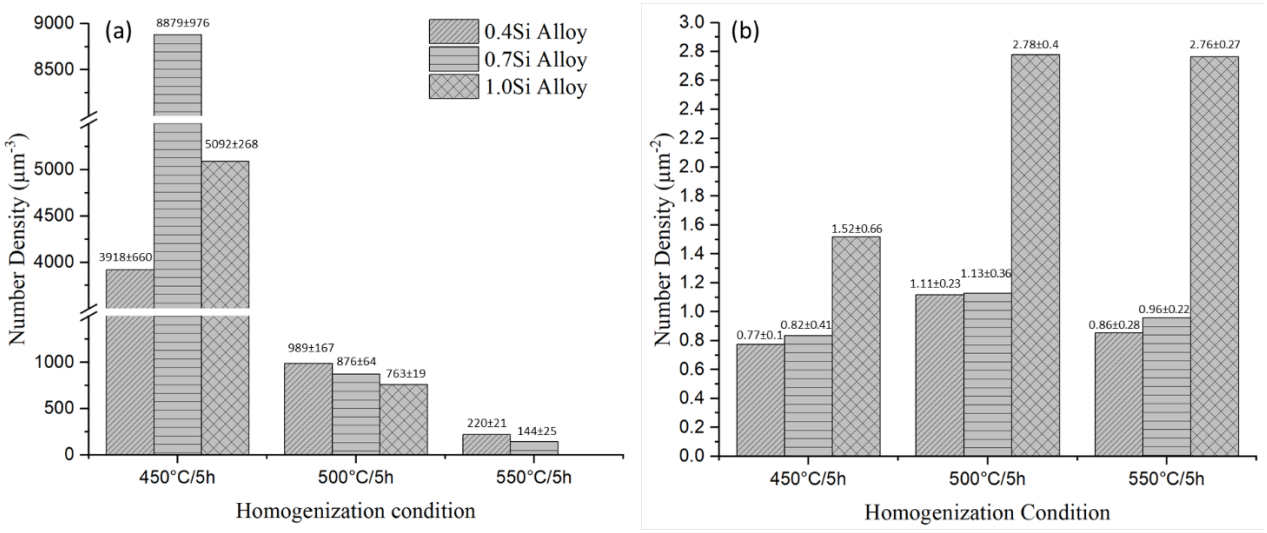

Figure 6. Number density of spherical dispersoids (a) and elongated dispersoids (b) for Si and homogenization variants

Figure 7 presents a schematic overview of the evolution of all precipitates across the range of Si contents. For a fixed Zr content, it is clear that Si can significantly affect the precipitation behavior of Zr-bearing dispersoids. It is reported that Si can enhance the Zr diffusion kinetics in the aluminum matrix,[16] and hence accelerate the precipitation and transformation of Zr-bearing dispersoids. In addition, Mg, that was increased with Si, was reported to increase the supersaturation of Zr in Al matrix which could enhance the nucleation of Zr-dispersoids.[34] At the lowest homogenization temperature (450 °C), large β-Mg_2Si and DO_{22}-$(Al,Si)_3(Zr,Ti)$ particles precipitated at the cell and grain boundaries, and fine Al_3Zr precipitated at cells/grain centers, forming dispersoid free zones (DFZs) close to cell and grain boundaries. For the 0.4Si alloy, the precipitation of spherical Al_3Zr dispersoids was quite sluggish, so the number density of Al_3Zr was relatively low with large DFZs. With increasing the Si to 0.7%, a remarkable increase in the precipitation of Al_3Zr dispersoids was observed, which was driven by the strong nucleation provided by Si atom clusters,[35] resulting in a much higher number density of Al_3Zr (Figure 6a) and narrow DFZs. At the highest level of Si (1.0%), the Al_3Zr dispersoids co-existed with a large

number density of DO_{22}-$(Al,Si)_3(Zr,Ti)$ dispersoids inside the cell/grain due to the transformation of dispersoids, and the DFZs were almost eliminated.

During high-temperature homogenization (550 °C), β-Mg_2Si particles in the cell/grain boundaries were completely dissolved, which provided more silicon to promote the precipitation of DO_{22}-$(Al,Si)_3(Zr,Ti)$. In 0.4Si and 0.7Si alloys, the elongated DO_{22} dispersoids were mainly concentrated at the cell/grain boundaries, while Al_3Zr dispersoids were located inside grains. Because of the increased Zr diffusion rate and associated coarsening at high temperatures, the Al_3Zr dispersoids were coarser with a lower number density than those formed after low-temperature homogenization. For the high Si alloy (1.0Si), a complete transformation of dispersoids was observed, resulting in the disappearance of $L1_2$-Al_3Zr and a uniform distribution of 100% elongated DO_{22} dispersoids in the matrix. In general, the nonhomogeneous distribution of each precipitate (Figure 7) is mainly related to the different segregation behavior of Zr and Si during solidification. For instance, Zr tends to be segregated and enriched inside the aluminum cell and grain as a consequence of the peritectic reaction in the Al-Zr system.[36] Therefore, the $L1_2$-Al_3Zr dispersoids tend to be localized at such regions where a high level of Zr supersaturation exists. Conversely, the depletion of Zr towards the boundary results in DFZ formation. On the other hand, Si tends to segregate near grain boundaries during solidification and has a relatively high diffusion rate.[26] Hence, β-Mg_2Si particles and DO_{22}-$(Al,Si)_3(Zr,Ti)$ dispersoids precipitate preferentially near grain boundaries. However, at the highest Si level and highest homogenization temperature (1.0%Si at 550 °C), DO_{22} dispersoids were predominant, producing a uniform distribution of elongated dispersoids in the matrix.

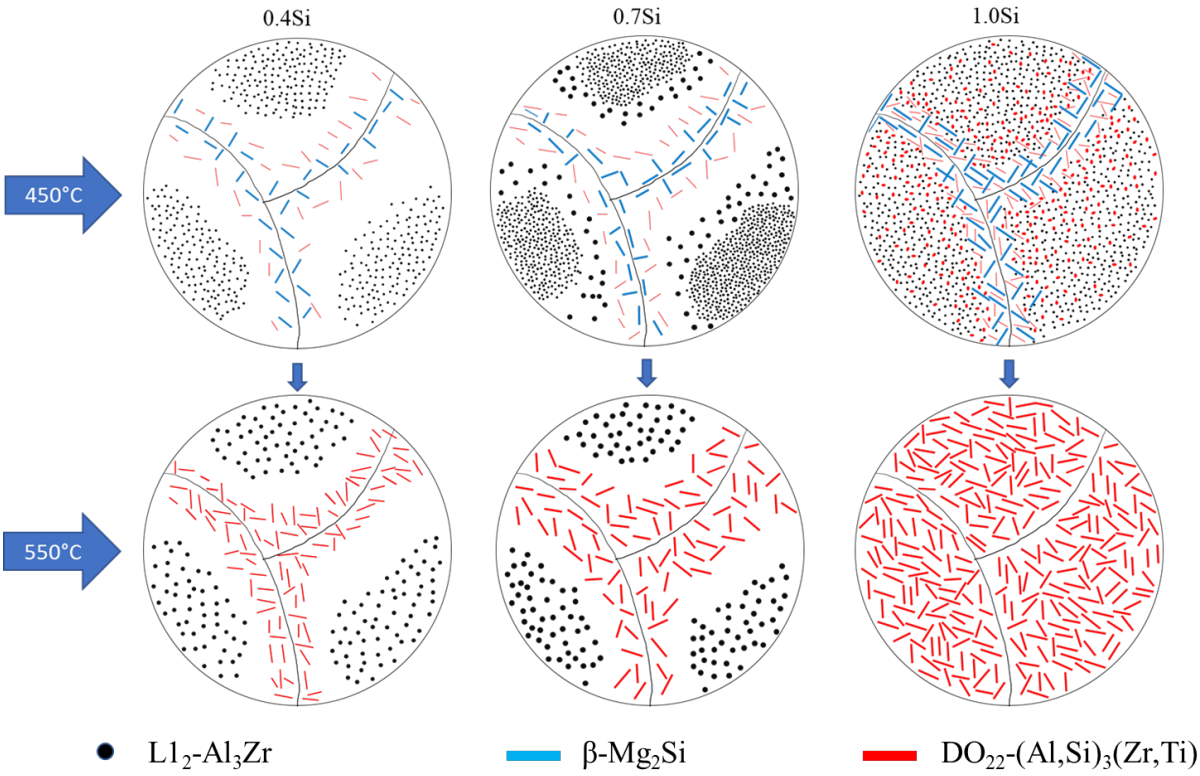

Figure 7. Schematic illustration of the evolution of Zr-bearing dispersoids, β-Mg_2Si and DFZs in different alloys during low- and high-temperature homogenization.

3.2. Hot deformation behavior

3.2.1. *Flow stress*

Figure 8 shows typical true stress-strain curves obtained in different Z conditions for the three alloys under different homogenization conditions. For all conditions, there is a sharp increase in the flow stress in the initial stage of compression until reaching the peak flow stress owing to strong work hardening. Subsequently, the softening mechanisms affected the flow stress curves with further deformation, which are dependent on the deformation condition, alloy composition and homogenization condition. The flow stress curves exhibited three trends: (1) a slow but continuous increase of the flow stress with increasing strain (arrow A), indicating the dominant effect of work hardening; (2) a steady-state (arrow B) where a plateau in the flow stress occurred, which is attributed to a dynamic balance between the work hardening and softening; (3) a decline

of the flow stress with increasing strain (arrow C), indicating the dominant effect of softening mechanisms. The 0.4Si alloy exhibited a continuous increase of the flow stress during high Z deformation (350 °C, 1.0 s^{-1}), indicating the dominant effect of work hardening rather than softening, while it exhibited steady state flow stress curves in the medium and high Z conditions regardless of the homogenization conditions. On the other hand, 0.7Si and 1.0Si alloys showed a slight dependency on the homogenization condition. For example, homogenization at 450 °C resulted in more work hardening as compared to higher temperatures, particularly at 550 °C. This effect was more apparent at high Z (350 °C, 1.0 s^{-1}) but reduced significantly at low Z (450 °C, 0.001s^{-1}). Such different behaviors are mostly related to the interactions between the dislocations and dispersoids during hot deformation. The high density of fine nanoscale Al_3Zr dispersoids that precipitated at low homogenization temperature appeared to be more effective to hinder the dislocation movement compared to large elongated DO_{22}-$(Al,Si)_3(Zr,Ti)$ dispersoids that precipitated at 550°C.

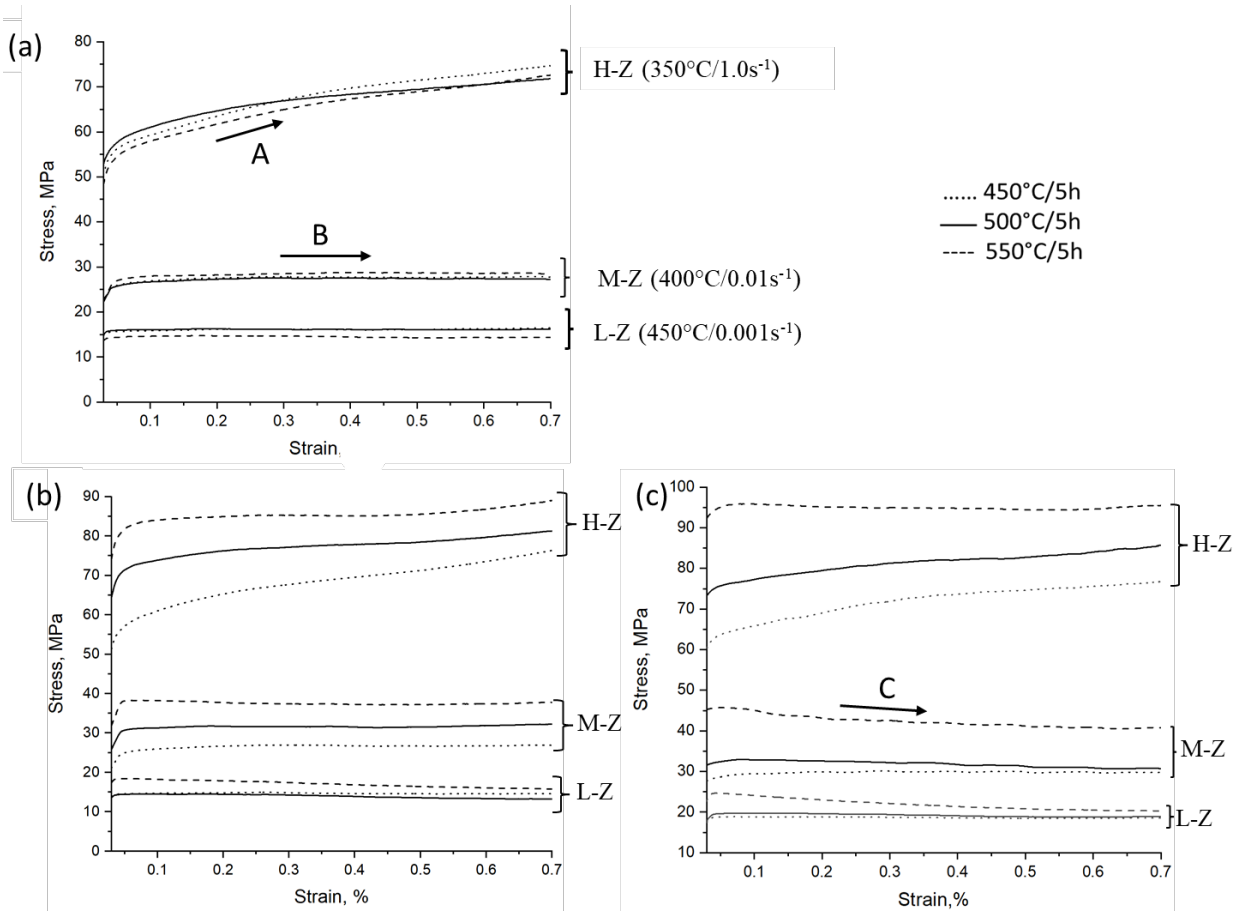

Figure 8. Typical flow curves in different Z conditions for (a) 0.4Si, (b) 0.7Si and (c) 1.0Si alloys under different homogenization conditions.

It can be seen from Figure 8 that the flow stress was primarily dependent on the hot deformation conditions (Z parameter). The higher the Z value, the higher is the flow stress. The highest flow stress was achieved in the high Z condition, where the temperature is relatively low (350 °C), and the strain rate is high (1.0 s^{-1}). By increasing the temperature to 450 °C and decreasing the strain rate to 0.001S^{-1} (low Z), the flow stresses significantly decreased. This is because the higher temperature facilitates the movement and annihilation of dislocations, while the lower strain rate provides sufficient time for the accumulation of activation energy.[37, 38] Figure 9 shows the flow stress values at high Z for the three alloys under different homogenization conditions, demonstrating the effect of alloy composition on the flow stress. For the samples

homogenized at 450 °C, the flow stress slightly increased with increasing Si from 0.4% to 1.0%. With increasing homogenization temperature, a significant increase in the flow stress could be observed from 0.4%Si to 1.0%Si. Notably, after homogenization at 550 °C, the flow stress increased from 73 MPa (0.4Si alloy) to 89 MPa (0.7Si alloy) and further to 95.6 MPa for the 1.0Si alloy. **Figure 10** shows the results of electrical conductivity (EC) measurements, which indicated the solid solution level of alloying elements (mainly Si and Mg) for each alloy. The EC decreases considerably with increasing Si content. A higher electrical conductivity corresponds to a lower solid solution level and vice-versa. By Comparing Figure 9 with Figure 10, it is reasonable to assume that the flow stress increase is closely related to the solid solution level of Si and Mg in the aluminum matrix. It is clear that the 0.4Si alloy has the lowest solid solution level, while the 1.0Si alloy exhibits the highest solid solution level for all homogenization conditions. Correspondingly, the 0.4Si alloy exhibited the lowest flow stress, while the 1.0Si alloy produced the highest flow stress (Figure 9).

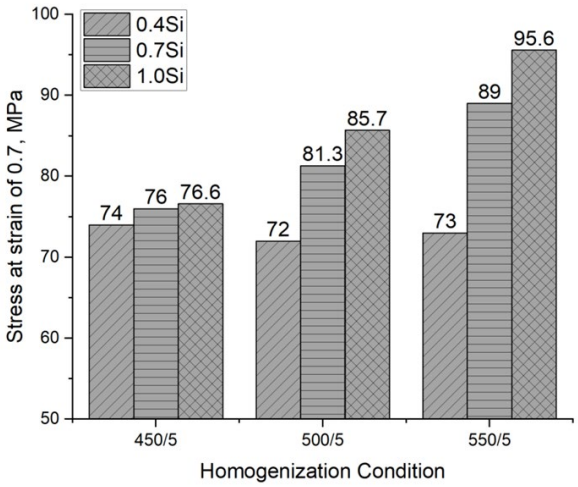

Figure 9. Flow stress at a strain of 0.7 in the high Z condition for the Si and homogenization variants

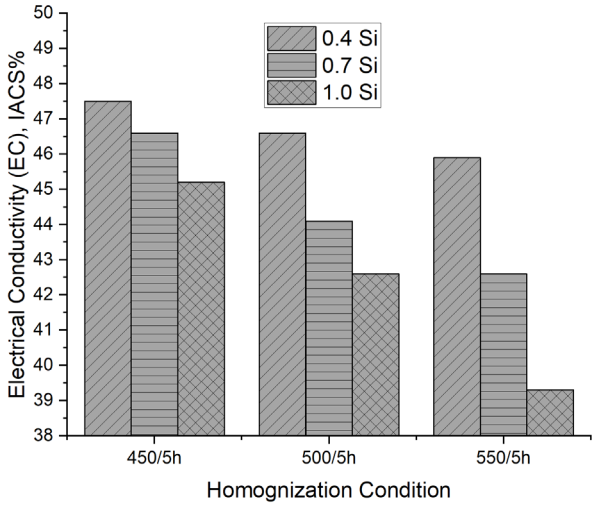

Figure 10. Electrical conductivity for the Si and homogenization variants

3.2.2. Microstructure evolution during deformation

To study the microstructure evolution during deformation, samples homogenized at 450 °C, and 550 °C were selected for investigation by the EBSD technique. **Figure 11** shows All-Euler maps for the three Si contents after compression testing in the high Z condition, while **Figure 12** displays All-Euler maps obtained in the low Z condition. A quantitative analysis of misorientation angle fractions was also performed, and the results are presented in **Figure 13**. In general, the three alloys showed quite similar deformed microstructures, exhibiting elongated grains perpendicular to the deformation direction.

In the high Z condition, a high number density of low and medium angle boundaries inside the elongated grains was observed, indicating a low dynamically recovered structure. The samples homogenized at high temperature (550 °C) exhibited a higher fraction of low angle boundaries for all alloys (Figure 13). This is more apparent in the case of 1.0Si, which showed a low angle boundary fraction of 54% for 450 °C against 62% for 550 °C. Such results agree with the flow stress values shown in Figure 9, where higher flow stress at high-Z condition was observed for the

samples homogenized at 550 °C. The high level of solutes at 550 °C may hinder the dislocation movement and create pile-ups,[39] which in turn reduces the rate of dynamic recovery and increases the fraction of low angle boundaries. On the other hand, no significant difference was observed between the low- and high-temperature homogenization conditions for the 0.4Si alloy. In addition, some tiny recrystallized grains were observed in the 0.7Si and 1.0Si alloys shown in Figure 11b and c, respectively (indicated by white arrows with the enlarged inset of c). These grains were observed along the initial grain boundaries, where large intermetallic particles are present. The homogenization at a low temperature (450 °C) was insufficient to dissolve large primary Mg_2Si particles, especially for 1.0Si, which has a large amount of these particles. The presence of large intermetallic particles and DFZs along grain boundaries could promote the nucleation of recrystallized grains in these regions. [40]

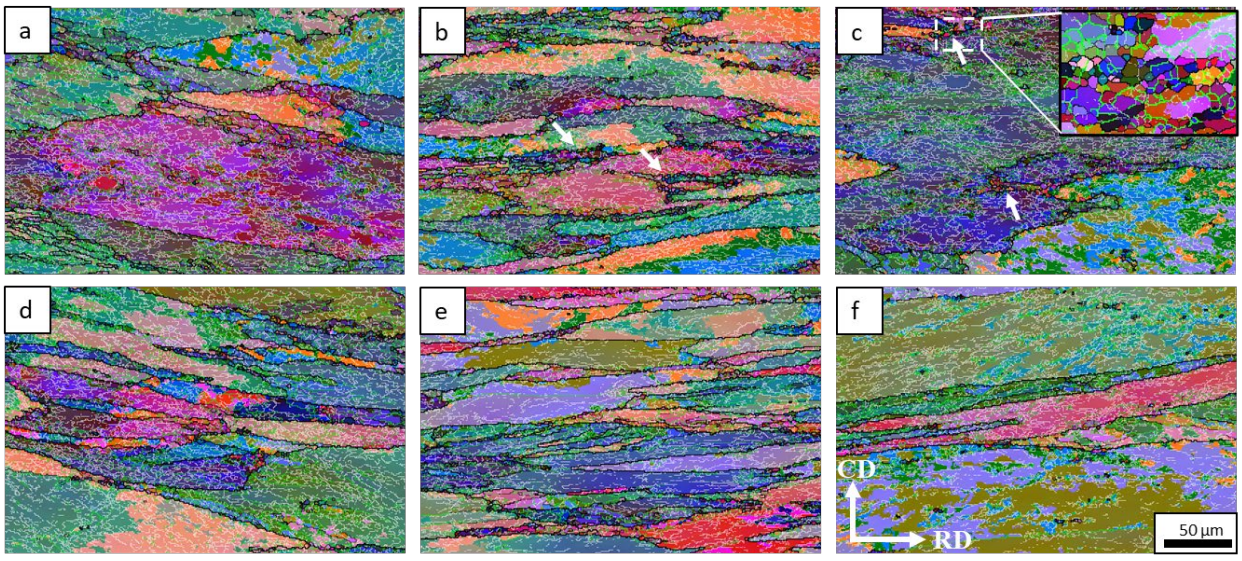

Figure 11. All-Euler orientation maps of as-deformed structures in the high Z condition (350 ^{o}C,1.0 s^{-1}) for: (a, d) 0.4Si, (b, e) 0.7Si and (c, f) 1.0Si alloys homogenized at (a-c) 450^{o}C/5h and (d-f) 550^{o}C/5h. Low angle (2^{o}-5^{o}), medium angle (6^{o}-15^{o}), and high angle boundaries (>15^{o}) were represented by white, green, and black lines, respectively. The arrows in (f) refer to the compression direction (CD) and radial direction (RD).

On the other hand, in the low Z deformation condition (450 °C, 0.001 s^{-1}), the substructure densities were significantly reduced with neatly organized boundaries within the elongated grains as an indication of an increasing level of DRV (Figure 12). A significant reduction of low angle boundaries was observed along with a significant increase in the fraction of medium and high angle boundaries relative to those at high Z (Figure13). It is known that high deformation temperature facilitates the migration of sub-grain and grain boundaries by accelerating the dislocation annihilation and rearrangement through climb and glide, resulting in a high rate of DRV.[41] Also, the lower strain rate allows more time for subgrain coalescence and growth. In the same deformation condition, the 0.4Si and 0.7Si exhibited similar fractions of low and medium angle boundaries, while the 1.0Si showed higher fractions of low and medium angle boundaries, indicating more restriction for boundary migration, and hence a lower DRV rate.

Regarding the effect of the homogenization temperature, 0.4Si showed almost the same structure in terms of the fraction of different grain boundaries for homogenization at 450 °C and 550 °C. Meanwhile, a slight difference was observed in 0.7Si alloy with a fraction of low and medium angle boundaries of 80% and 84% for homogenization at 450 °C and 550 °C, respectively. However, an apparent difference between the different homogenization conditions was exhibited by 1.0Si with a fraction of low and medium angle boundaries of 83% vs. 92% for homogenization at 450 °C and 550 °C, respectively. Such results are also in conformity with the flow stress obtained at low Z, where the highest values were achieved by the samples homogenized at 550 °C, particularly for 1.0Si.

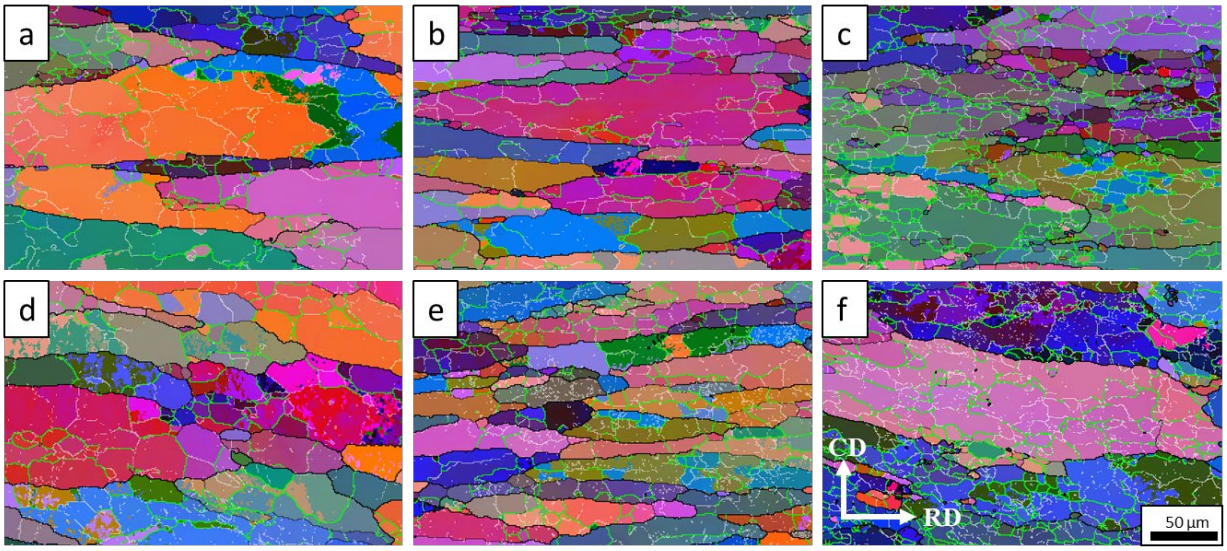

Figure 12. All-Euler orientation maps of as-deformed structures in the low Z condition (450°C,0.001 s^{-1}) for: (a, d) 0.4Si, (b, e) 0.7Si and (c, f) 1.0Si alloys homogenized at (a-c) 450ºC/5h and (d-f) 550ºC/5h. Low angle (2°-5°), medium angle (6°-15°), and high angle boundaries (>15°) were represented by white, green, and black lines, respectively. The arrows in (f) refer to the compression direction (CD) and radial direction (RD).

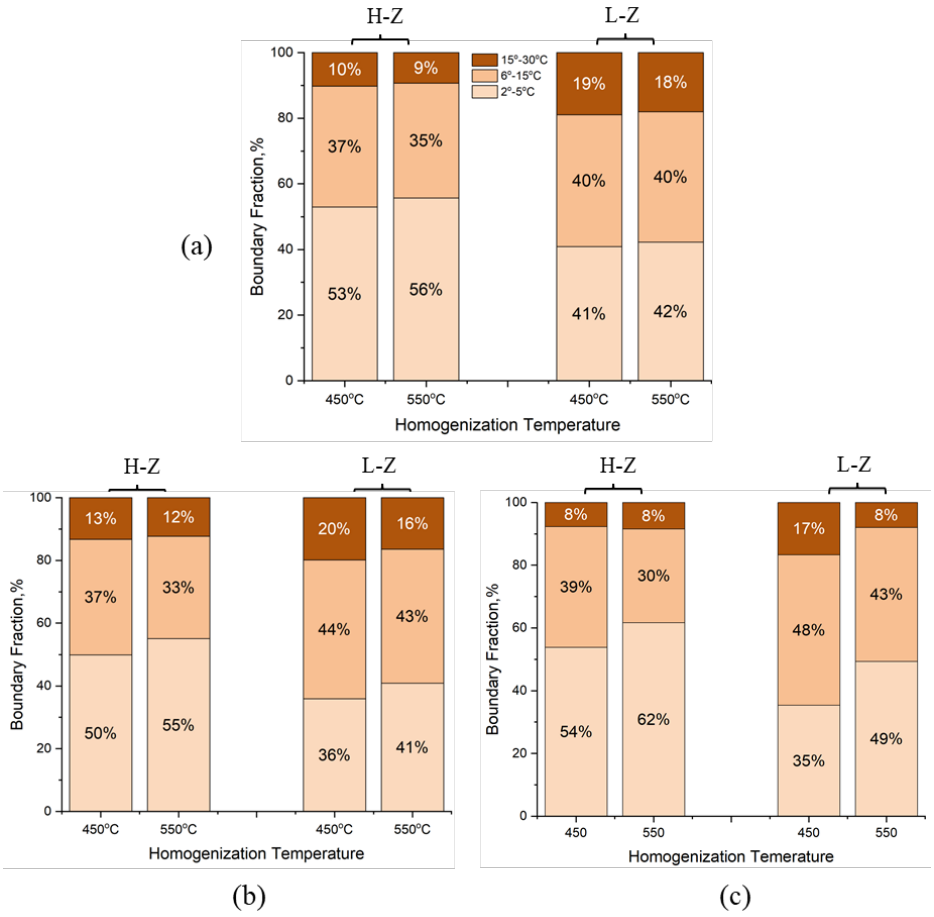

Figure 13. Misorientation angle fractions after deformation at high Z and low Z (a) 0.4Si, (b) 0.7Si and (c) 1.0Si alloys homogenized at different temperatures.

3.3. Recrystallization resistance during post-deformation annealing

The samples homogenized at 450 °C and 550 °C and deformed in the high Z condition (350 °C, 1.0 s^{-1}) were selected to evaluate the recrystallization resistance at two different annealing temperatures 500 °C and 540 °C for 1h holding time because such samples possessed similar microstructure (deformed and less recovered) as the starting microstructure (Figure 10). **Figure 14 and 15** show All-Euler EBSD maps after annealing at 500 °C and 540 °C, respectively. In addition, the recrystallized area fractions for each condition were quantitatively analyzed, and the results are shown in **Figure 16**. After 500 °C annealing, a partially recrystallized microstructure with some newly formed grains was observed in all alloys (Figure 14). These new grains were

characterized by high angle boundaries and were free of internal substructures. The recrystallized grains were found to be preferentially nucleated and grown along grain boundaries where the dispersoid-free zones are located. In general, the samples homogenized at 450 °C (Figure 14a-c) exhibited much lower recrystallized fractions compared to the samples homogenized at 550 °C (Figure 14d-f), for instance, 8-30% recrystallized fraction at 450 °C homogenization vs. 28-63% recrystallized fraction at 550 °C homogenization (Figure 16). Furthermore, at a given homogenization temperature, the 1.0Si exhibited the highest recrystallization resistance compared to the other two alloys (0.4Si and 0.7Si). For instance, only 8.3% and 28% recrystallized area fractions were measured for homogenization at 450 °C and 550 °C respectively, while the other two alloys (0.4Si and 0.7Si) exhibited much higher values (Figure 16).

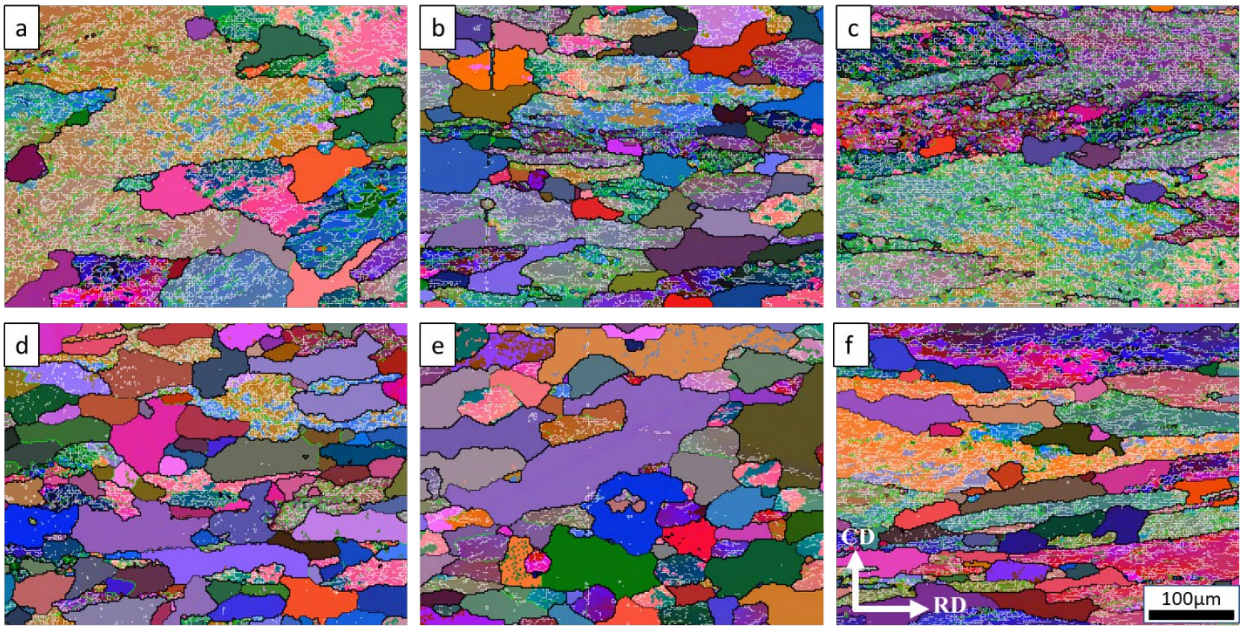

Figure 14. All-Euler orientation maps after annealing at 500°C/1h for: (a, d) 0.4Si, (b, e) 0.7Si and (c, f) 1.0Si alloys homogenized at (a-c) 450ºC/5h and (d-f) 550ºC/5h. The arrows in (f) refer to the compression direction (CD) and radial direction (RD).

Increasing the annealing temperature to 540 °C resulted in a significant increase in the recrystallized fraction (>50%) for all conditions, as shown in Figure 15. The high annealing temperature provides more thermal activation energy for dislocations to move and bypass the obstacles, and hence the recrystallization can easily propagate. Compared to annealing at 500 °C, the samples homogenized at 450 °C (Figure 15a-c) still had lower recrystallized fractions relative to the samples homogenized at 550°C (Figure 15d-f), but the difference in recrystallization fractions was reduced (Figure 16). Again, the 1.0Si exhibited the lowest recrystallization fraction among the three alloys under both homogenization conditions.

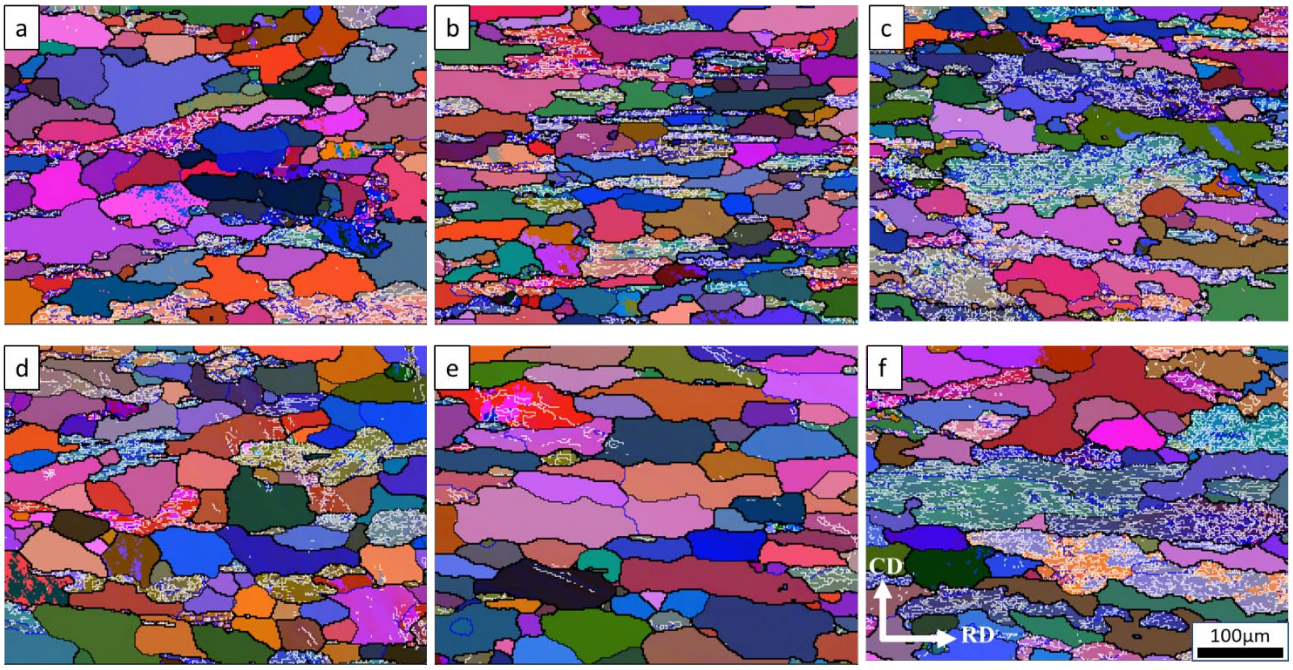

Figure 15. All-Euler orientation maps after annealing at 540°C/1h for: (a, d) 0.4Si, (b, e) 0.7Si and (c, f) 1.0Si alloys homogenized at (a-c) 450°C/5h and (d-f) 550°C/5h. The arrows in (f) refer to the compression direction (CD) and radial direction (RD).

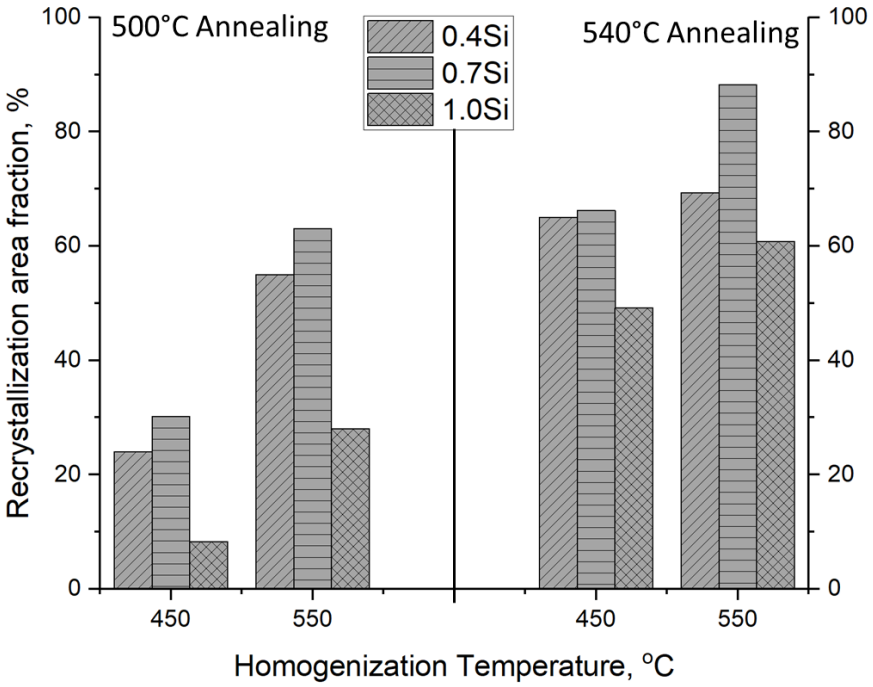

Figure 16. Recrystallization area fractions after annealing at 500°C/1h and 540°C/1h for Si and homogenization variants.

The EBSD results show that both alloy composition and homogenization condition have a significant impact on the static recrystallization during post-deformation annealing. These mainly relate to the precipitation of Zr-bearing dispersoids ($L1_2$ and DO_{22}) during homogenization which affects the migration of grain boundaries through the Zener drag forces. The pinning efficiency of such dispersoids is determined by their size, number density, and distribution. After annealing at 500 °C, the samples homogenized at 450 °C exhibited low recrystallized fractions (Figure 16). The fine dense $L1_2$-Al_3Zr dispersoids precipitated during low-temperature homogenization were reported to have better performance on static recrystallization inhibition compared to the large elongated DO_{22} dispersoids.[42]

On the other hand, the distribution of dispersoids and the dispersoids free zone (DFZ) are critical to provide an even pinning effect across the grains.[43] The 0.4Si and 0.7Si alloys exhibited

a non-uniform distribution of Al_3Zr dispersoids and large DFZs with limited large elongated dispersoids (Figure 7). Therefore, some areas were adjacent to grain boundaries without dispersoids, giving a locally reduced pinning effect. In contrast, the 1.0Si alloy showed a uniform distribution of Al_3Zr and/or DO_{22}-$(Al,Si)_3(Zr,Ti)$ dispersoids within the grain interior and very limited DFZs at grain boundaries, resulting in an efficient and uniform pinning effect across the microstructure. Consequently, it exhibited the best recrystallization resistance among the three alloys studied.

By increasing the annealing temperature to 540 °C, higher thermal activation energy was provided, resulting in a higher level of recrystallization in all conditions. Similar to annealing at 500 °C, less recrystallization occurred in the case of low-temperature homogenization (450 °C). However, the difference between low and high-temperature homogenization for the same alloy was significantly reduced (Figure 16). One reason is that the high-temperature annealing could also promote the transformation of the dispersoids from $L1_2$ to DO_{22}. A part of $L1_2$-Al_3Zr dispersoids formed during low-temperature homogenization (450 °C) would transform to DO_{22}-$(Al,Si)_3(Zr,Ti)$. This would result in a similar pinning effect to that produced at high temperature (550 °C).

4. Conclusions

The evolution of Zr-bearing dispersoids in 6xxx alloys with a range of Si levels and the effect of these dispersoids on the hot deformation and recrystallization resistance have been studied under different homogenization conditions. The following conclusions can be drawn:

(1) Two types of Zr-bearing dispersoids were mainly observed depending on the alloy composition and homogenization condition: fine spherical $L1_2$-Al_3Zr and large elongated DO_{22}-$(Al,Si)_3(Zr,Ti)$ dispersoids.

(2) The precipitation of $L1_2$-Al_3Zr dispersoids occurred primarily at low homogenization temperatures. Increasing Si content and homogenization temperature promoted the transformation of $L1_2$-Al_3Zr to DO_{22}-$(Al,Si)_3(Zr,Ti)$. For the highest Si content and temperature (1.0%Si at 550 °C), the elongated DO_{22} dispersoids were predominant.

(3) The flow stress was controlled by the solid solution level and hot deformation parameters rather than by the dispersoid characteristics, and hence the flow stress increased with the Si level.

(4) The fine $L1_2$-Al_3Zr dispersoids with a high number density formed during low-temperature homogenization resulted in higher recrystallization resistance during post-deformation annealing compared to the large DO_{22}-$(Al,Si)_3(Zr,Ti)$ dispersoids.

(5) The high Si alloy (1.0%) exhibited superior recrystallization resistance during post-deformation annealing as compared to the low silicon alloys (0.4-0.7%), regardless of the homogenization condition. This was attributed to the more uniform distribution of dispersoids and minimal dispersoid-free zones.

Acknowledgments

The authors would like to acknowledge the financial support of the Natural Sciences and Engineering Research Council of Canada (NSERC) under the Grant No. CRDPJ 514651-17 and Rio Tinto Aluminum through the Research Chair in the Metallurgy of Aluminum Transformation at University of Quebec at Chicoutimi.

Data availability

The raw/processed data required to reproduce these findings cannot be shared at this time due to legal or ethical reasons.

References

[1] O. Reiso, Mater. Forum. **2004**, 28, 32.

[2] A. Poznak, D. Freiberg, P. Sanders, in: Fundamentals of Aluminium Metallurgy, Woodhead Publishing, **2018**, 333.

[3] M. Cai, G.J. Cheng, JOM. **2007**, 59, 58.

[4] Y. Birol, Met. Mater. Int. **2016**, 20, 727.

[5] C. Poletti, T. Wójcik, C. Sommitsch, Metall. Mater. Trans. A. **2012**, 44, 1577.

[6] C. Li, K. Liu, X.G. Chen, J. Mater. Sci. Technol. **2020**, 39, 135.

[7] G.W. Zhang, H. Nagaumi, Y. Han, Y. Xu, C.M. Parish, T.G. Zhai, Mater. Sci. Forum. **2017**, 877, 172.

[8] Z. Guo, G. Zhao, X.G. Chen, Mater. Charact. **2015**, 102, 122.

[9] Y. Ding, K. Gao, S. Guo, S. Wen, H. Huang, X. Wu, Z. Nie, D. Zhou, Mater. Charact. **2019**, 147, 262.

[10] K.E. Knipling, D.C. Dunand, D.N. Seidman, Acta Mater. **2008**, 56, 1182.

[11] Y.-l. Deng, Y.-y. Zhang, L. Wan, A.A. Zhu, X.-m. Zhang, Metall. Mater. Trans. A. **2013**, 44, 2470.

[12] Z. Guo, G. Zhao, X.G. Chen, Mater. Charact. **2016**, 114, 79.

[13] Y. Meng, J. Cui, Z. Zhao, L. He, Mater. Charact. **2014**, 92, 138.

[14] S. Babaniaris, M. Ramajayam, L. Jiang, R. Varma, T. Langan, T. Dorin, Mater. Sci. Eng., A. **2020**, 793.

[15] C. Wolverton, Acta Mater. **2007**, 55, 5867.

[16] N.Q. Vo, D.C. Dunand, D.N. Seidman, Mater. Sci. Eng., A. **2016**, 677, 485.

[17] T. Gao, A. Ceguerra, A. Breen, X. Liu, Y. Wu, S. Ringer, J. Alloys Compd. **2016**, 674, 125.

[18] L. Litynska, D. Abou-Ras, G. Kostorz, J. Dutkiewicz, J Microsc. **2006**, 223, 182.

[19] A. Chamanfar, M.T. Alamoudi, N.E. Nanninga, W.Z. Misiolek, Mater. Sci. Eng., A. **2019**, 743, 684.

[20] S. Liu, Q. Pan, H. Li, Z. Huang, K. Li, X. He, X. Li, Mater. Sci. **2019**, 54, 4366.

[21] H.J. McQueen, S. Spigarelli, M.E. Kassner, E. Evangelista, Hot Deformation and Processing of Aluminum Alloys, CRC Press, **2016**.

[22] A. Rollett, G.S. Rohrer, J. Humphreys, Recrystallization and related annealing phenomena, Newnes, **2017**.

[23] S. Andersen, H. Zandbergen, J. Jansen, Acta Mater. **1998**, 46, 3283.
[24] C.D. Marioara, S.J. Andersen, J. Jansen, H.W. Zandbergen, Acta Mater. **2003**, 51, 789.
[25] S.M. Allen, Philos. Mag. A. **1981**, 43, 325.
[26] H. Seo, J. Gu, K. Park, Y. Jung, J. Lee, W. Chung, Met. Mater. Int. **2013**, 19, 433.
[27] S. Tsunekawa, M.E. Fine, Scr. metall. mater. **1982**, 16, 391.
[28] Z.-H. Jia, J.-P. Couzinié, N. Cherdoudi, I. Guillot, L. Arnberg, P. Åsholt, S. Brusethaug, B. Barlas, D. Massinon, Trans. Nonferrous Met. Soc. China. **2012**, 22, 1860.
[29] T. Sato, A. Kamio, G.W. Lorimer, Mater. Sci. Forum. **1996**, 217-222, 895.
[30] A.V. Mikhaylovskaya, A.G. Mochugovskiy, V.S. Levchenko, N.Y. Tabachkova, W. Mufalo, V.K. Portnoy, Mater. Charact. **2018**, 139, 30.
[31] F. Zupanič, C. Gspan, J. Burja, T. Bončina, Mater. Today Commun. **2020**, 22, 100809.
[32] M.F. Ashby, L.M. Brown, Philos. Mag. A. **2006**, 8, 1083.
[33] F. Schmid, I. Weißensteiner, M.A. Tunes, T. Kremmer, T. Ebner, R. Morak, P.J. Uggowitzer, S. Pogatscher, Acta Mater. **2021**, 15, 100997.
[34] J.D. Robson, P.B. Prangnell, Mater. Sci. Eng., A. **2003**, 352, 240.
[35] S.H. Wu, H. Xue, C. Yang, P.M. Cheng, P. Zhang, J. Kuang, J.Y. Zhang, G. Liu, J. Sun, Mater. Sci. Eng., A. **2021**, 812, 141150.
[36] Z. Jia, G. Hu, B. Forbord, J.K. Solberg, Mater. Sci. Eng., A. **2007**, 444, 284.
[37] X. Kai, C. Chen, X. Sun, C. Wang, Y. Zhao, Mater. Des. **2016**, 90, 1151.
[38] H.R. Ezatpour, M. Haddad Sabzevar, S.A. Sajjadi, Y. Huang, Mater. Sci. Eng., A. **2014**, 606, 240.
[39] X. Qian, N. Parson, X.G. Chen, Can. Metall. Q. **2020**, 59, 189.
[40] X. Qian, N. Parson, X.G. Chen, J. Mater. Sci. Technol. **2020**, 52, 189.
[41] S.H. Liu, Q.L. Pan, M.J. Li, X.D. Wang, X. He, X.Y. Li, Z.W. Peng, J.P. Lai, Mater. Des. **2019**, 184, 108181.
[42] A. Elasheri, E.M. Elgallad, N. Parson, X.G. Chen, J. Mater. Eng. Perform. **2021**, 30, 7851.
[43] L.-M. Wu, W.-H. Wang, Y.-F. Hsu, S. Trong, J. Alloys Compd. **2008**, 456, 163.